PHYSICAL REVIEW B **85**, 195414 (2012)

Dynamics, anisotropy, and stability of silicon-on-insulator dewetting fronts

F. Leroy, F. Cheynis, T. Passanante, and P. Müller
Centre Interdisciplinaire de Nanoscience de Marseille (CINaM) CNRS UMR 7325, Aix-Marseille Université, Case 913 Campus de Luminy, 13288 Marseille Cedex 9, France

(Received 1 March 2012; published 8 May 2012; corrected 29 May 2012)

We report on the anisotropy of solid state dewetting of straight fronts of $Si(001)/SiO_2$ obtained by electron beam lithography. The $\langle 110\rangle$ front is stable. It recedes with formation of a faceted rim that thickens in a layer-by-layer mode kinetically limited by 2D nucleation on the top facet of the rim. The front position and the height of the rim respectively obey $\sim t^{0.37\pm0.03}$ and $\sim t^{0.38\pm0.02}$ power laws. The $\langle 100\rangle$ front is unstable. It breaks down then recedes at constant velocity. The $\langle 100\rangle$ front instability is characterized by the formation of void fingers whose tips retract at constant shape with a kinetics limited by the mass transfer from the void tip to the Si fingers. The conditions of stability of a straight front are discussed in the light of recent theoretical models. New perspectives for controlling solid dewetting are opened.

DOI: 10.1103/PhysRevB.85.195414 PACS number(s): 68.55.−a, 68.35.Md, 68.37.Nq, 68.60.Dv

I. INTRODUCTION

Metastable thin solid films, when annealed, can agglomerate into an assembly of nanocrystals. This dewetting process is a limit for the fabrication of advanced devices.[1] Conversely, it is also a common method to produce self-organized nanocrystals used in several nanoscale processes.[2,3] As such, a fundamental understanding of the mechanisms governing solid state dewetting is of particular relevance. In recent years, ultrathin crystalline silicon-on-insulator (SOI) film has been recognized as a model system for studying solid state dewetting.[4–7] Spontaneous dewetting of single-crystalline SOI thin film is generally initiated by heterogeneous nucleation of voids at randomly distributed defects followed by their growth. These voids are surrounded by a thickening rim at the origin of a fingering instability. At last the fingers break down into 3D nanoislands self-organized into a regular array.[4,8–19] Most of the experiments on solid state dewetting concern such spontaneous dewetting of continuous thin films except for two studies on line-shaped[20] or square-shaped[21] nanostructures. All these experiments show a strong anisotropy of the SOI dewetting leading to the formation of $\langle 110\rangle$-sided voids as well as to the line-up of Si islands in the dewetted state. The origin of this anisotropy has been discussed on the basis of *ex situ* examination of the final dewetted state (see for instance Refs. 12 and 15) but also on the basis of preliminary real-time observations (see for instance Refs. 7 and 13) for heterogeneous nucleation and SOI nanopatterns.[20,21] However, heterogeneous nucleation is not controlled *by definition*,and the dewetting of nanopatterns appears to be influenced by the pattern shape and by the amount of Si available in such small SOI structures.[20,21] It is thus necessary to go beyond these first approaches by studying the dewetting of true 2D films initiated at straight edges whose crystallographic orientation is perfectly controlled. It is all the more important that theoretical predictions[17,22–25] concern simple geometry as the dewetting from straight fronts. Moreover, contrary to classical theoretical investigations based on the isotropic continuum surface-diffusion model of Mullins,[26] the most recent models highlight several crystallinity effects such as the anisotropy of dewetting velocity and the role of 2D nucleation on the rim thickening[22–24] that cannot be accurately studied through heterogeneous dewetting or dewetting of nanopatterns.

In this paper, we present the first real-time observation of the dewetting of SOI films from artificial well-oriented edges obtained by lithography. Using various edge orientations, we have been able to investigate the anisotropy of the instability of solid dewetting straight fronts with a peculiar emphasis on kinetics. We show that (i) the $\langle 110\rangle$-oriented edge retracts as $x \sim t^{0.37\pm0.03}$ accompanied by a rim-thickening $h \sim t^{0.38\pm0.02}$ (t being time) and (ii) the $\langle 100\rangle$ edges are highly unstable against the formation of perpendicular elongated Si structures called in the following Si fingers, separated by void fingers. The void tips propagate at constant shape with $x \sim t$ and $dh/dt = 0$. For stable $\langle 110\rangle$ orientations the kinetics is governed by the 2D nucleation on top of the rim. For unstable $\langle 100\rangle$ orientations, kinetics is governed by the mass transfer from the void-finger tip to the Si fingers. At last we show how a stable $\langle 110\rangle$ front may be destabilized by local defects.

II. EXPERIMENT

The experiments have been performed with a low-energy electron microscope (Elmitec LEEM III) at pressures $< 10^{-9}$ Torr. The samples are bonded SOI (CEA-Leti, France) composed of stress-free single-crystal Si(001) films (22 ± 2 nm thick) on a 150-nm-thick amorphous SiO_2 film.[16] The samples are cleaned according to a published recipe.[27] We measure dewetting by LEEM in bright field, dark field, and tilted bright imaging modes.[28] In these modes images are formed either from a reflected spot, 1/2-order diffraction beam associated with the Si(100)-2×1 surface reconstruction or from a tilted incident beam. As adjacent terraces have orthogonal surface reconstructions dark field and tilted bright field modes give rise to a bright-dark contrast that reveals the step organization at the surface. LEEM image sequences are recorded at a fixed rate (0.3–10 Hz) to form a movie of the dewetting process. The LEEM measurements show simultaneously the micrometer-scale structure of the dewetting front, the nanoscale motion of surface atomic steps, and 2D nucleation events. The motion of steps during the dewetting process is a clear indication of a surface diffusion mediated process and allows us to draw connections between macroscopic evolution and atomistic processes. Well-oriented trenches have been fabricated by electron beam lithography. For this purpose we use a PPMA-950K electrosensitive positive resin deposited by spin coating and insolated on predefined regions by a 20 keV electron gun. The insolated resin is then dissolved by the MIBK:IPA (1:3) chemical solvent. Finally, trenches are dug by reactive ion etching by means of a radio frequency source (15 W) which generates a plasma in the SF6 low-pressure gas suitable for the silicon etching. The depth of the trenches allows us to reach the underlying SiO_2 substrate.

III. STRUCTURE AND DYNAMICS OF THE DEWETTING FROM STRAIGHT FRONTS

A. Dewetting phenomenon

Let us first describe qualitatively the morphology of fronts dewetting for various orientations of in-plane trenches. Whereas for continuous SOI film annealed at $T > 750\,^{\circ}\mathrm{C}$ the dewetting starts at morphological defects,[4,8–19,29] the dewetting of the patterned films starts at the edges of the artificial trenches. Due to the fourfold symmetry of the Si(001) surface, in-plane trench orientations between 0° and 45° with respect to the $\langle 110\rangle$ direction have been studied. According to the orientation of the front edges, we observe two different dewetting mechanisms (Fig. 1 and Fig. 2). If the film edge is aligned along the $\langle 110\rangle$ direction, the dewetting occurs by the retraction of a straight front [Figs. 2(a) to 2(d)]. For other crystallographic directions, a breakdown of the trench edge is observed and the dewetting proceeds via the formation of void fingers separated by Si fingers (see Fig. 1 for fronts oriented at 10°, 20°, 30°, and 45° with respect to the $\langle 110\rangle$ direction). In the following $\langle 110\rangle$ straight fronts will be called stable fronts while fingered fronts will be called unstable fronts. This is illustrated in Fig. 2 where are reported a LEEM sequence of a dewetting trench constituted by $\langle 110\rangle$ and $\langle 100\rangle$ segments [Figs. 2(a) to 2(d)] and a macroscopic view of a partially dewetted trench [Fig. 2(e)]. The dewetted zones essentially develop from the $\langle 100\rangle$ segments which illustrates the strong anisotropy of the dewetting velocity $V_{\langle 100\rangle} \gg V_{\langle 110\rangle}$. Notice that the Si fingers periodically shed mass, forming 3D nanoislands (dots in Fig. 1 and 5).

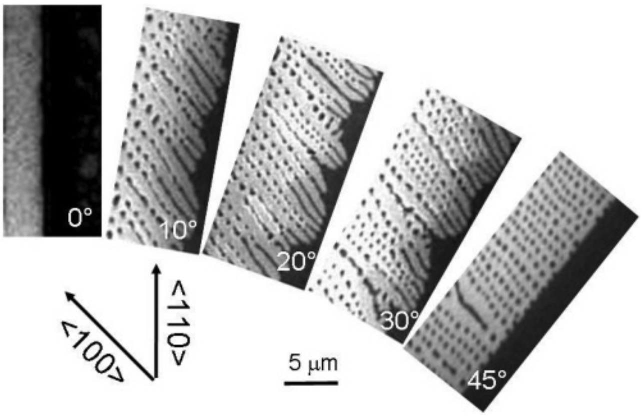

FIG. 1. LEEM images (bright field) of UHV-annealed SOI artificial fronts having different edge orientation with respect to the $\langle 110\rangle$ direction. The Si material is dark and the SiO_2 substrate is bright. The dewetting fronts form $\langle 100\rangle$-oriented Si fingers whatever the initial orientation of the dewetting fronts. The breakdown of the Si fingers, separated by $\lambda \approx 0.8\ \mu$m, forms 3D nanoislands (dots) aligned in the $\langle 100\rangle$ direction. Notice that the nanoisland distribution is more narrow when the Si fingers are perpendicular to the front edge (Si thickness: 22 nm, temperature: 825 °C).

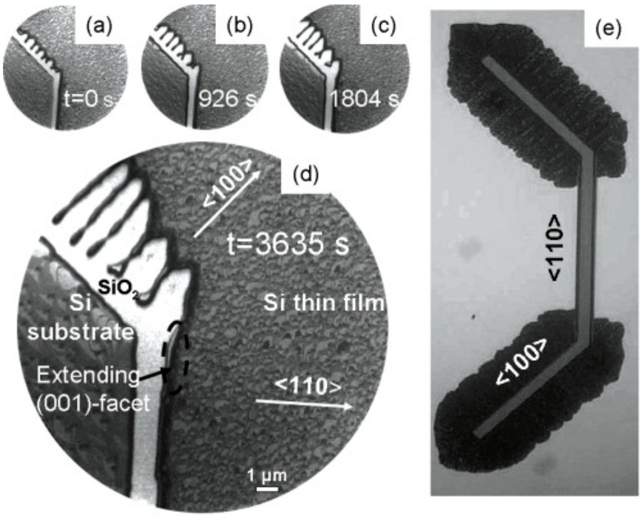

FIG. 2. (a) to (d): LEEM sequence (dark field mode, same field of view of 15 μm) obtained during dewetting of an artificial trench formed by $\langle 110\rangle$- and $\langle 100\rangle$-oriented branches: The $\langle 110\rangle$ edge remains straight while the $\langle 100\rangle$ edge recedes by formation of perpendicular Si fingers separated by void fingers. (e) Macroscopic picture (obtained by optical micrograph) of the partial dewetting at 825 °C of an artificial trench with one $\langle 110\rangle$- and two $\langle 100\rangle$-oriented branches dug by lithography (trench width: 2 μm, total length: 75 μm, Si thickness: 22 nm).

In the following we focus on the kinetics of the stable $\langle 110\rangle$ and unstable $\langle 100\rangle$ fronts. We will focus on the stationary state in which both stable and unstable fronts recede at constant morphology. In both cases we have measured, *in situ*and in real time, the kinetics of edge retraction as well as the kinetics of the local rim thickening at $T = 825\,^{\circ}\mathrm{C}$ for a 22-nm-thick SOI film.

B. Kinetics of stable receding fronts

Let us study the retraction of $\langle 110\rangle$-oriented edges. Figure 2 reveals the key feature of the process: The $\langle 110\rangle$-oriented edge is stable and remains straight during the dewetting process. During dewetting, the silicon expelled from the trench edge is transferred to a 3D rim (see AFM profile in Fig. 3). LEEM movies show that this rim is topped by a (001) atomic 1×2 or 2×1 reconstructed flat facet. Indeed, in dark field conditions, the top facet appears either dark or bright according to the diffraction spot—(1/2,0) or (0,1/2)—selected for imaging (Fig. 3). The flatness of the top facet of the rim is confirmed by AFM (Fig. 3). The stabilization of the $\langle 110\rangle$ front edge orientation is highlighted by the progressive lateral extension of the (001) top facet along the front edge direction (Fig. 2).

As the rim recedes, its top facet alternatively flashes from bright to dark (inset of Fig. 4), which means that the rim thickens in a layer-by-layer growth mode with alternatively

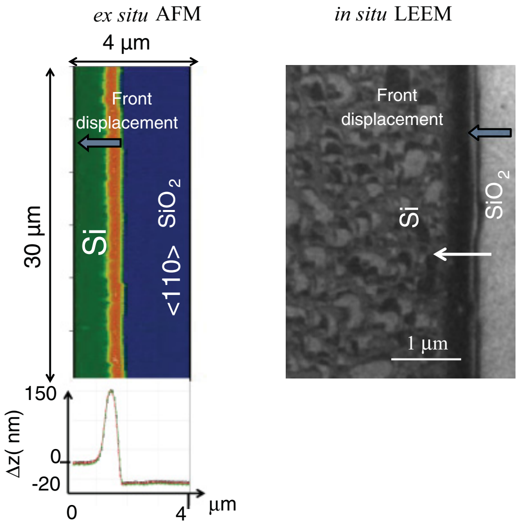

FIG. 3. (Color online) AFM and LEEM (dark field conditions) pictures of a stable ⟨110⟩ front. Notice in LEEM the bright contrast of the top of the rim characteristic of an atomically flat surface exhibiting a (1 × 2) reconstruction. AFM profile shows the 3D rim with its flat top facet.

TABLE I. Theoretical prediction and asymptotic behaviors. All the results have been obtained by considering mass conservation.

Box-shaped rim model (Refs. 7 and 19)
$dx/dt = D_s c_{eq} \Omega^2 / w a^2 h^2$
If $w = C^{te}$: $x \sim t^{1/3}$, $h \sim t^{1/3}$ If $w/h = C^{te}$: $x \sim t^{0.4}$, $h \sim t^{0.2}$ If $h = C^{te}$: $x \sim t^{1/2}$ If h and $w = C^{te}$: $x \sim t$

1×2 then 2×1 surface reconstructions. The time dependence of the front position $x(t)$, as well as the time dependence of the rim thickening $h(t)$ (obtained by counting the number of flash events), is reported in Fig. 4. It is observed that the rim retracts as $\Delta x_{\text{exp}}(t) = (190 \pm 20) t^{0.37\pm0.03}$ while simultaneously the global thickening behavior exhibits a $\Delta h_{\text{exp}}(t) = (6 \pm 2) t^{0.38\pm0.02}$ behavior (with lengths expressed in nanometers and time in minutes). These results partially differ from numerical predictions obtained with continuous models[22] that predict $h(t) \sim t^{1/5}$ and $x(t) \sim t^{2/5}$. In Refs. 7 and 19 we have developed a 1D analytical model in which we assume that the velocity of a front edge is equal to the thermodynamic driving force times a surface-diffusion-based mobility. More precisely, our analytical expression reads $dx/dt = K\,(\mu/k_B T)$ with $K = (D_s c_{eq} \Omega^2 / h w a^2)$ where Ω and a^2 respectively are the volume and surface area of an atom, D_s the diffusion constant, c_{eq} the surface adatom fraction at equilibrium, and h and w the height and the width of the rim. The quantity $\mu = E_s/h$ is the local chemical potential per unit volume at the edge of the rim[30] with $E_s = \gamma_{Si} + \gamma_{int} - \gamma_{Ox}$ a parameter that controls the wetting properties of the film (surface energy γ_{Si}) on the substrate (surface energy γ_{Ox}) with γ_{int} the interfacial energy.[7] The velocity expression dx/dt can be analytically integrated in a few asymptotic situations reported in Table I.

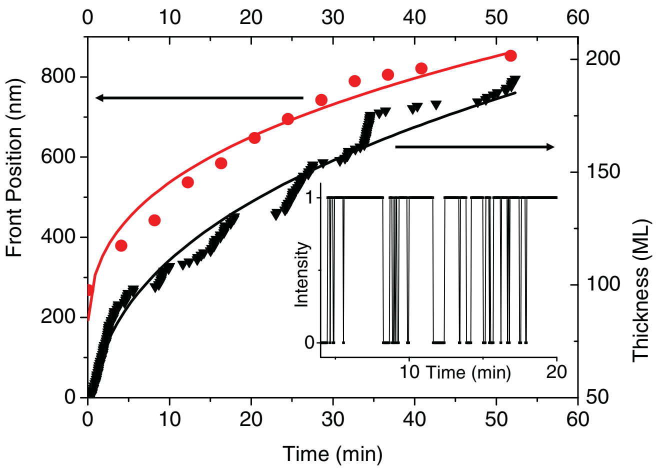

FIG. 4. (Color online) Front position (red circles) and rim height (black triangles) versus time (dots: experimental data, continuous curve: best fits). Inset: LEEM intensity versus time, recorded on the top facet of the rim, illustrating its layer-by-layer thickening.

Comparison of experimental data and asymptotic power laws reported in Table I suggests that the rim recedes at constant width. More precisely, using all available material data, $E_s = 14$ eV nm^{-2} from Ref. 19, $D_s c_{eq} = 7 \times 10^6$ nm^2 s^{-1} valid at $T = 825\,^\circ$C,[19,31] initial film thickness $h_0 = 22$ nm, a rim width $w \approx 400$ nm (measured by AFM), $\Omega = a_0^3$, $a = a_0\sqrt{2}/2$ valid for Si(001) surface with $a_0 = 0.543$ nm the Si crystallographic parameter, we obtain $x(t) \approx 190\,t^{1/3}$ and $h(t) \approx 10\,t^{1/3}$ in quite nice agreement with the experimental behaviors: $\Delta x_{\text{exp}}(t) \approx 190 t^{0.37\pm0.03}$ and $\Delta h_{\text{exp}}(t) \approx 6 t^{0.38\pm0.02}$.

However, LEEM experiments give further information on the thickening mechanism. Indeed when analyzing the bright-to-dark blinking (see inset of Fig. 4) it can be noticed that the residence time τ_{res} in the dark or bright state, which corresponds to the time needed to nucleate a 2D nucleus, is longer than the completion time of a new terrace. In other words LEEM data show that the rim thickening proceeds via nucleation of 2D islands followed by island growth that quickly invades the whole facet. The same thickening mechanism is at the origin of 3D island thickening induced by dewetting in various other systems.[5,32–34] In this context we could expect to obtain a better fit considering that the limiting step is the two-dimensional nucleation on top of the rim facet. However, in our system, the classical capillary theory of nucleation cannot be applied. Indeed, though the Si(001) surface contains two types of steps having two different free energies, at 825 °C one can use the mean step energy $\beta = 6$ meV/Å[35] so that assuming circular nucleating islands, the critical nucleus radius $(\beta/a\mu)$ deduced from the classical capillary theory is too small (roughly a dimer) and thus out of its domain of validity. The growth rate of the rim thus should be closer to a Hertz-Knudsen type law[36,37] $dh/dt \propto \mu/k_B T$, which is the form of the analytical expression given in Table I. Finally, notice that we measure $\tau_{\text{res}}^{1\times2}/\tau_{\text{res}}^{2\times1} = 1.50 \pm 0.02$ irrespective of the film thickness which means independently of the slowing down of the rim thickening (Fig. 4). This asymmetry is due to the diffusion anisotropy on 1×2 and 2×1 surfaces since, using the nucleation theory, there comes $\tau_{\text{res}}^{1\times2}/\tau_{\text{res}}^{2\times1} = D^{2\times1}/D^{1\times2}$

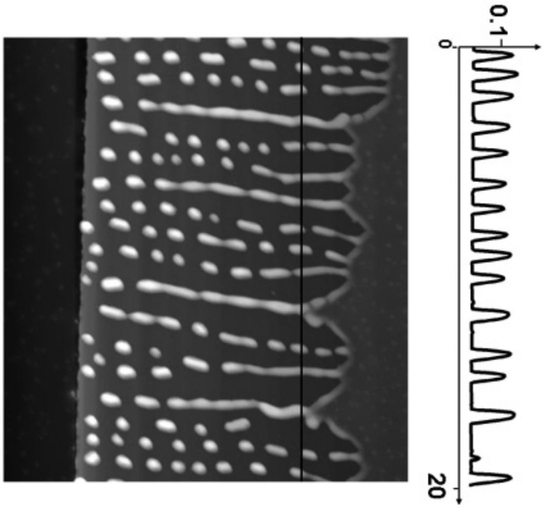

FIG. 5. AFM picture (right) and height profile (left) of an unstable $\langle 100 \rangle$ front. The AFM profile (vertical and horizontal units are μm) shows that the finger instability is associated with a local height instability. Notice that the fingers locally form bunches. The wider the finger width inside a bunch, the smaller the bunch velocity.

where D^i are the diffusion coefficients for adatoms on the terrace $i = 1 \times 2$ or $i = 2 \times 1$. Thanks to the layer-by-layer growth mode of the rim, the adatom flux leaving the front is thus alternatively oriented along or perpendicular to the dimers of the reconstructed top facet. The 2D nucleation rate is thus influenced by the dimer orientation with respect to the flux of diffusing adatoms.

C. Kinetics of unstable receding fronts

Let us now consider the case of $\langle 100 \rangle$-oriented fronts. Figure 2 shows sequential images from the retraction of a 22-nm-thick SOI film with $\langle 100 \rangle$-oriented edge. The $\langle 100 \rangle$ front is unstable; it locally slows down and forms elongated structures called Si fingers into which the mass of the film is efficiently transferred (Fig. 5). Other regions of the dewetting fronts recede at constant velocity [$x(t) \sim t$] and govern the velocity of the mean front. This steady state regime is characterized by a constant shape of the void finger tip. From AFM and LEEM we can infer that the void finger tip is the intersection of two adjacent $\{111\}$ and/or $\{113\}$ facets. It is observed that the rim at the void finger tip recedes with a constant height ($\sim$ 30 nm) smaller than the height of the surrounding Si fingers. This confirms, in agreement with predictions of Table I, that void fingers receding at constant shape (constant height h and constant width w) have a constant velocity: $x(t) \sim t$. Obviously in this case there is no more local mass conservation but only a global mass conservation where the Si expelled from the void tip feeds the Si fingers leading to a periodic height variation of the receding front (Fig. 5). At a constant temperature, the period λ of the Si fingers remains constant during the whole dewetting process. We also find that the velocity of the front depends on the void-finger density: $V_{\text{fing}} \sim \lambda^{-1}$. This means that the evolution of an unstable front can be mainly captured by simply considering the local behavior of a void tip. At first sight, the dewetting dynamics is thus simply limited by the mass transfer from each void tip to its neighboring Si fingers (for a discussion see Ref. 7). However collective behaviors involving neighbored fingers exist. It results that Si fingers may form bunches of 2–5 fingers (Fig. 2 and Fig. 5) of local velocity $V_{\text{bunch}} \sim \lambda_{\text{loc}}^{-1}$ where λ_{loc} is the interfinger distance inside the bunch.

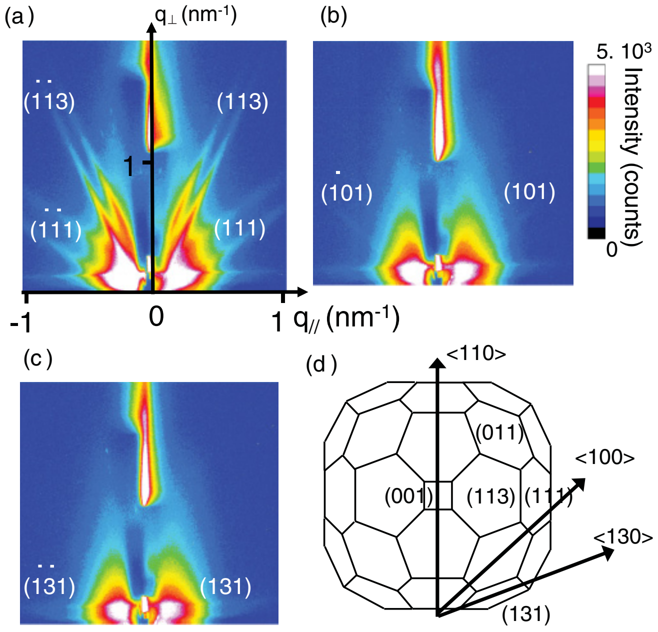

FIG. 6. (Color online) GISAXS patterns recorded with incident beam parallel to $\langle 110 \rangle$ (a), $\langle 100 \rangle$ (b), and $\langle 130 \rangle$ (c) directions. In (d) is sketched the Si equilibrium shape with its characteristic $\{011\}$, $\{001\}$, $\{113\}$, and $\{111\}$ microfacets as well as the directions of the fronts described in the text.

IV. STABILITY CONDITIONS AND SURFACE FACETING

The presence of facets on the dewetting fronts has been characterized by grazing incidence small angle x-ray scattering (GISAXS) at the European Synchrotron Facility in Grenoble, France. We report in Figs. 6(a) to 6(c) the GISAXS patterns recorded with incident beam respectively parallel to the $\langle 110 \rangle$, $\langle 100 \rangle$, and $\langle 130 \rangle$ directions. In the case of the $\langle 110 \rangle$ direction, we observe scattering rods (with respect to the surface normal)

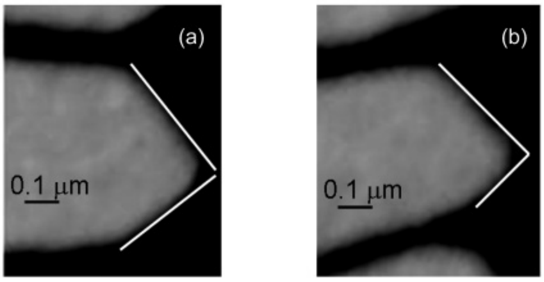

FIG. 7. Void-tip structure (bright field mode; dark: Si material, bright SiO_2 substrate). (a) Symmetric void tip formed by two symmetric microfronts oriented along $\{110\}$ directions (bright lines) characteristic of a perfectly $\langle 100 \rangle$-oriented dewetting front. (b) Asymmetric void-tip characteristic of a dewetting front slightly misoriented from the $\langle 100 \rangle$ direction, with two asymmetric microfronts oriented along $\{110\}$ directions (bright lines) at the origin of local deviation of the Si finger orientation.

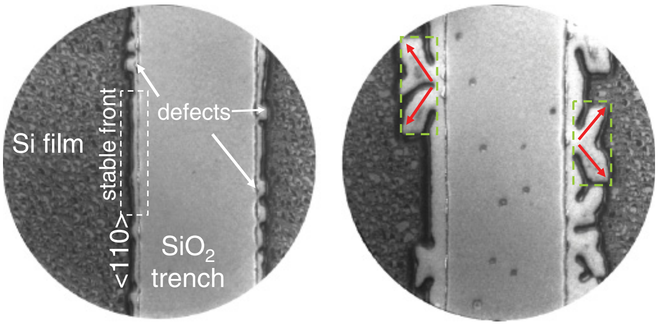

FIG. 8. (Color online) Instability of a ⟨110⟩-oriented front initiated by the formation of squared defects whose corners are at the origin of the formation of ⟨100⟩- and ⟨010⟩-oriented fingers (red arrows).

associated with the presence of well-developed {111} and {113} facets. These facets belong to the Si equilibrium shape[7,38,39] and have for common zone axis the ⟨110⟩ front direction. For the ⟨100⟩ direction, the only facet is a small {011} facet. The strong stability of the ⟨110⟩ front with respect to the ⟨100⟩ front is thus clearly associated with the presence of facets parallel to the front edge leading to a fully faceted ⟨110⟩ front. Since {111} and {113} facets stabilize the ⟨110⟩ front we could expect that other directions, such as ⟨310⟩ fronts, could be stabilized by {311} facets. However, as already reported by Danielson,[16] this is not the case. This is mainly due to the small size of these facets [Fig. 6(c)].

The sketch of the Si equilibrium shape reported in Fig. 6 illustrates the strong stability of the ⟨110⟩ front with respect to the ⟨100⟩ front. The {111} and {113} facets that stabilize the ⟨110⟩ front favor a decomposition of the ⟨100⟩ front into two microfronts oriented along the ⟨110⟩ directions. These microfronts are the sides of the tip of the void fingers formed by the unstable front in experiments as reported in Fig. 7(a). Notice that if a local deviation of the front orientation occurs, the corresponding void tips are no more formed by two symmetric microfronts but a local asymmetry appears and leads to local deviations of the finger orientation [Fig. 7(b)].

All these experimental observations are in agreement with recent models of solid dewetting mechanisms where, on the basis of diffusion-limited mass transport and 2D nucleation on the rim facet, it has been predicted that front instability emerges for rough front orientations, while fronts along faceted orientations remain stable.[24]

Finally, the results reported in Fig. 8 allow us to understand how a ⟨110⟩ stable front may be destabilized by defects. In most cases, small defects which locally modify the front velocity are spontaneously healed. However, in a few cases, the pinning leads to the formation of square-shaped defects (Fig. 8) limited by ⟨110⟩ stable sides. The corners of these squared defects behave as precursors of ⟨100⟩-oriented void fingers limited by ⟨110⟩ microfronts. Thus a defective ⟨110⟩ front may be destabilized, forming after a long enough time an assembly of ⟨100⟩- and ⟨010⟩-oriented Si fingers separated by periodic void fingers [see for instance Fig. 4(c) in Ref. 19]. Notice that such a local destabilization of ⟨110⟩ fronts naturally occurs in the case of heterogeneous dewetting on defected zones, where the ⟨110⟩-oriented sides of the opening voids are at the origin of finger formation.[7] As shown in Fig. 7 local deviations of the side orientation lead to local deviations of the finger orientation. This is the reason heterogeneous dewetting leads to a majority of ⟨100⟩-oriented fingers but also other possible orientations, among which is ⟨130⟩-oriented fingers locally stabilized by the presence of {131} facets along the fingers.[15,32]

V. CONCLUSION

In conclusion, SOI dewetting exhibits a strong anisotropy. The ⟨110⟩ fronts are stable. They recede by forming a faceted rim that thickens in a layer-by-layer mode. While classical theories based on isotropic continuum surface diffusion correctly capture the main tendencies ($x \sim t^{\alpha}$, $h \sim t^{\beta}$), they fail to find the accurate value of the exponent which is driven by the 2D nucleation mechanism on top of the faceted rim. The ⟨100⟩ fronts are highly unstable. Again, classical theories fail to predict the correct behavior while our analytical expression reported in Refs. 7 and 19 agrees with most of the experimental results. The model could be improved by taking into account the 2D nucleation on top of the rim facet but beyond the usual capillary approximation. The stability condition is governed by the presence of crystallographic atomically flat facets having the front direction as a common zone axis. In the absence of such facets the front is unstable and forms ⟨100⟩-oriented fingers the period of which is kinetically selected since the interfinger distance has been shown[7] to correspond to the most unstable mode predicted by the classical linear analysis stability based on the surface diffusion model.[22,26] Finally, this study opens new perspectives since the dewetting may be delayed or the Si nanoisland formation may be controlled by selecting the front orientation. Indeed, unless defective, ⟨110⟩ fronts limit dewetting while ⟨100⟩ fronts dewet with formation of well-ordered Si nanoislands.

ACKNOWLEDGMENTS

We thank E. Bussmann and O. Pierre-Louis for fruitful discussions. We also acknowledge J. C. Barbé and co-workers from CEA LETI for SOI fabrication, Frederic Bedu and Igor Ozerov from CINaM-Planete for lithography support, as well as J. Eymery and N. Blanc for their help during our beam time access at the ESRF. This work is supported by ANR PNano Grant DEFIS (ANR 08-Nano-036) and PACA Grant Nanosurf.

---

[1] C. Jahan, O. Faynot, L. Tosti, and J. Hartmann, J. Cryst. Growth **280**, 530 (2005).
[2] S. V. Kodambaka, J. Tersoff, and F. Ross, Science **316**, 729 (2007).
[3] H.-C. Yuan, B. Yang, J. Simmons, M. Marcus, Z. Ma, and M. Eriksson, Proc. SPIE **5971**, 597118 (2005).
[4] D. T. Danielson, D. Sparacin, J. Michel, and L. Kimerling, J. Appl. Phys. **100**, 083507 (2006).
[5] K. Thurmer and N. C. Bartelt, Phys. Rev. Lett. **100**, 186101 (2008).
[6] G. Capellini, G. Ciasca, M. de Seta, A. Notargiacomo, F. Evangeslisy, and M. Nardone, J. Appl. Phys. **105**, 093525 (2009).

[7] F. Cheynis, E. Bussmann, F. Leroy, T. Passanante, and P. Müller, Phys. Rev. B **84**, 245439 (2011).

[8] Y. Ono, M. Nagase, M. Tabe, and Y. Takahashi, Jpn. J. Appl. Phys. **34**, 1728 (1995).

[9] R. Nuryadi, Y. Ishikawa, and M. Tabe, Appl. Surf. Sci. **159**, 121 (2000); **160**, 121 (2000).

[10] B. Legrand, V. Agache, J. Nys, V. Senez, and D. Stievenard, Appl. Phys. Lett. **76**, 3271 (2000).

[11] B. Legrand, V. Agache, T. Melin, J. Nys, V. Senez, and D. Stievenard, J. Appl. Phys. **91**, 106 (2002).

[12] R. Nuryadi, Y. Ishikawa, Y. Ono, and M. Tabe, J. Vac. Sci. Technol. B **20**, 167 (2002).

[13] B. Yang, P. Zhang, D. E. Savage, M. G. Lagally, G. H. Lu, M. Huang, and F. Liu, Phys. Rev. B **72**, 235413 (2005).

[14] P. Sutter, W. Ernst, Y. Choi, and E. Sutter, Appl. Phys. Lett. **88**, 141924 (2006).

[15] E. Dornel, J. C. Barbé, F. de Crecy, G. Lacolle, and J. Eymery, Phys. Rev. B **73**, 115427 (2006).

[16] D. T. Danielson, Ph.D. thesis, University of California, Berkeley, 2008.

[17] E. Dornell, Ph.D. thesis, Université de Grenoble, 2007.

[18] Y. Fan, R. Nuryady, Z. Burhadunin, and M. Tabe, Jpn. J. Appl. Phys. **47**, 1461 (2008).

[19] E. Bussmann, F. Cheynis, F. Leroy, P. Müller, and O. Pierre-Louis, New J. Phys. **13**, 043017 (2011).

[20] Y. Ishikawa, Y. Imai, H. Ikeda, and M. Tabe, Appl. Phys. Lett. **83**, 3162 (2003).

[21] Y. Ishikawa, M. Kumezawa, R. Nuryadi, and M. Tabe, Appl. Surf. Sci. **190**, 11 (2002).

[22] W. Kan and H. Wong, J. Appl. Phys. **97**, 43515 (2005).

[23] O. Pierre-Louis, A. Chame, and Y. Saito, Phys. Rev. Lett. **103**, 195501 (2009).

[24] M. Dufay and O. Pierre-Louis, Phys. Rev. Lett. **106**, 105506 (2011).

[25] J. Ye and C. V. Thompson, Phys. Rev. B **82**, 193408 (2010).

[26] W. Mullins, J. Appl. Phys. **28**, 333 (1957).

[27] E. Bussmann, F. Cheynis, F. Leroy, and P. Müller, IOP Conf. Ser.: Mater. Sci. Eng. **12**, 012016 (2010).

[28] E. Bauer, Rep. Prog. Phys. **57**, 895 (1994).

[29] Z. Burhanudin, R. Nuryadi, Y. Ishikawa, M. Tabe, and Y. Ono, Appl. Phys. Lett. **87**, 121905 (2005).

[30] O. Pierre-Louis, A. Chame, and M. Dufay, Eur. Phys. J. B **77**, 5763 (2010).

[31] M. E. Keefe, C. C. Umbach, and J. M. Blakely, J. Phys. Chem. Solids. **55**, 965 (1994).

[32] K. Thurmer, E. D. Williams, and J. E. Reutt-Robey, Phys. Rev. B **68**, 155423 (2003).

[33] K. Man, Q. Guo, and M. Altman, Surf. Sci. **600**, 1080 (2006).

[34] E. J. Luber, B. C. Olsen, C. Ophus, and D. Mitlin, Phys. Rev. B **82**, 085407 (2010).

[35] N. C. Bartelt, R. M. Tromp, and E. D. Williams, Phys. Rev. Lett. **73**, 1656 (1994).

[36] H. Hertz, Ann. Phys. (Berlin) **17**, 193 (1882).

[37] M. Knudsen, Ann. Phys. (Berlin) **47**, 697 (1915).

[38] J. Bermond, J. Métois, X. Egea, and F. Floret, Surf. Sci. **330**, 48 (1995).

[39] P. Müller and J.-J. Métois, Thin Solid Films **517**, 65 (2008).